Deriving flow velocity and initial concentration from Liesegang-like patterns

Chong Liu[1], Victor M. Calo[2], Klaus Regenauer-Lieb[3,4], Manman Hu[1]

[1]Department of Civil Engineering, The University of Hong Kong, Hong Kong, China
[2]School of Electrical Engineering, Computing, and Mathematical Sciences, Curtin University, P.O. Box U1987, Perth, WA 6845, Australia
[3]WA School of Mines: Minerals, Energy and Chemical Engineering, Curtin, Bentley, WA 6102, Australia
[4]School of Minerals and Energy Resources Engineering, UNSW, Sydney, NSW 2052, Australia

Key Points:

- Rich Liesegang-like patterns are replicated by varying flow velocities and initial conditions;
- A new class of inclined bands identified in a very narrow flow velocity and low concentration regime;
- Pattern precisely characterizes flow velocity and concentration when observed;

Corresponding author: Manman Hu, mmhu@hku.hk

Abstract

Zebra rocks, characterized by their striking reddish-brown stripes, rods, and spots of hematite (Fe-oxide), showcase complex self-organized patterns formed under far-from-equilibrium conditions. Despite their recognition, the underlying mechanisms remain elusive. We introduce a novel advection-dominated phase-field model that effectively replicates the Liesegang-like patterns observed in Zebra rocks. This model leverages the concept of phase separation, a well-established principle governing Liesegang phenomena. Our findings reveal that initial solute concentration and fluid flow velocity are critical determinants in pattern selection and transition. We quantitatively explain the spacing and width of a specific Liesegang-like pattern category. Furthermore, the model demonstrates that vanishingly low initial concentrations promote the formation of oblique patterns, with inclination angles influenced by rock heterogeneity. Additionally, we establish a quantitative relationship between band thickness and geological parameters for orthogonal bands. This enables the characterization of critical geological parameters based solely on static patterns observed in Zebra rocks, providing valuable insights into their formation environments. The diverse patterns in Zebra rocks share similarities with morphologies observed on early Earth and Mars, such as banded iron formations and hematite spherules. Our model, therefore, offers a plausible explanation for the formation mechanisms of these patterns and presents a powerful tool for deciphering the geochemical environments of their origin.

Plain Language Summary

Zebra rocks, known for their unique red and brown stripes and spots, hold clues to how similar patterns formed on early Earth and Mars. We have developed a new model to explain how these intriguing patterns form. The model suggests that the flow of fluids and the initial amount and location of dissolved iron-oxide (rust) in water plays a big role in shaping the final Zebra rock design. The speed of the flow and the initial amount of rust can create different stripe and spot patterns, just like the ones in Zebra rocks. By studying these rocks, we can potentially decipher fluid flow scenarios of ancient environments on both Earth and Mars.

1 Introduction

When geological systems are far from equilibrium, self-organization processes can form geochemical patterns autonomously (Ortoleva et al., 1987; L'Heureux, 2013; Wang et al., 2015; Al-Ghoul & Sultan, 2019; C. Liu et al., 2022, 2023a; Yatsuda et al., 2023; Qiu et al., 2024). Heterogeneity of geological materials and systems as well as complicated boundary conditions can make the observed patterns rich in information about the geological environments in which they are formed, particularly concerning fluid migration and initial conditions. In this contribution we develop a theory and method to use these patterns to provide a window into the past of planetary evolution.

One example of extensively studied pattern formation is the formation of variable hematite (Fe-oxide) on early Earth and Mars, including the Zebra rock formation, Precambrian banded iron formations (BIFs), Mississippi-Valley-type (MVT) ores, and others (Wang et al., 2009, 2015; C. Liu et al., 2023a). Field evidence suggests that groundwater flows influence the formation of Fe-oxide precipitation bands and that BIFs may reflect the changing composition of the oceanic crust (Kawahara et al., 2022; Wang et al., 2009). Additionally, concretions formed in Jurassic Navajo Sandstone have been proposed as a terrestrial analog to hematite spherules detected by the rover Opportunity at the Meridiani Planum site on Mars (Chan et al., 2004; Arvidson et al., 2014; Yoshida et al., 2018). Therefore, a better understanding of the pattern-forming processes in rocks and minerals can reveal valuable information about the geological environment on early

Earth and Mars, including the possibility of aqueous environments on Mars and the ability to invert fluid flow velocity and initial solute concentration on early Earth.

We study the Zebra Rock pattern in the northern region of Western Australia, which exhibits a unique and highly noticeable rhythmic concentration of hematite (Kawahara et al., 2022). Among all hematite banding patterns, none are as distinct and rich as the Zebra rock patterns. Thus, the Zebra rock formation is an excellent analog for various pattern-forming processes associated with subsurface environmental evolution. Zebra rock formation contains reddish-brown bands, rods, and elliptical spots on a white or light-colored background, as shown in Figure 1. In our earlier work, we linked Zebra rock formation to the Liesegang phenomenon, a process where supersaturation, nucleation (formation of solid particles), and depletion compete to create banded patterns (C. Liu et al., 2023a, 2023b). This connection was made because some Zebra rock patterns look similar to Liesegang bands. However, classic Liesegang bands typically show increasing band thickness and spacing as they form. Zebra rocks, on the other hand, exhibit a wider variety of patterns. To differentiate these, we refer to the Zebra rock patterns as Liesegang-like patterns throughout this study.

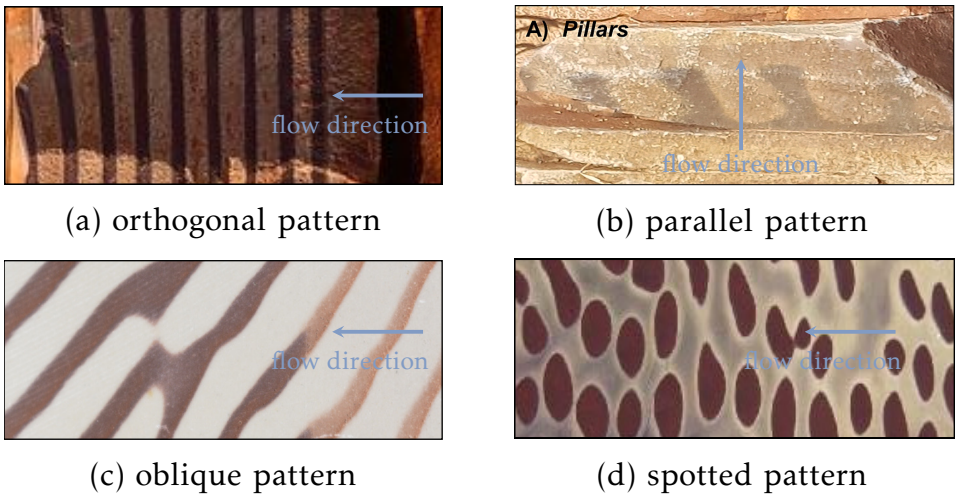

Figure 1. Rich patterns appear in Zebra rocks in the northern region of Western Australia: (a) orthogonal pattern; (b) parallel pattern (after Coward et al. (2023)); (c) oblique pattern; and (d) spotted patterns.

The fundamental Liesegang precipitation model helps to explain the forming mechanism of Zebra rocks (Loughnan & Roberts, 1990; Kawahara et al., 2022; Coward et al., 2023; C. Liu et al., 2023a). However, there are many other hypotheses regarding their origin, including alternating sedimentation either in marine environments (Larcombe, 1926) or ripple trough (Geidans, 1981), ferronematic liquid crystals (Mattievich et al., 2003), acid-sulfate soil weathering in conjunction with redox (Retallack, 2021).

Recently, acidic-hydrothermal alterations have been suggested to form Liesegang-like patterns behind a moving front of concentrated iron (Kawahara et al., 2022). However, this theory faces several challenges in explaining the diverse Zebra rock patterns: (i) the Liesegang theory predicts only simple band or ring patterns, while Zebra rocks exhibit a wider variety, including horizontal, vertical, and slanted stripes; (ii) diffusion-driven Liesegang patterns typically form over a small area. The theory has difficulties in explaining the vast, multi-layered patterns observed in the Ediacaran Ranford Formation, spanning over 45 kilometers (Coward et al., 2023); (iii) the Liesegang model is

limited in explaining pattern shape variations and cannot generate the spotted or rod-shaped patterns commonly seen in Zebra rock formations (Coward et al., 2023).

In an earlier contribution, we aimed to overcome some limitations of the Liesegang model, using the Cahn-Hilliard model to describe the mineral precipitation in a phase separation model in binary mixtures (C. Liu et al., 2023a). In this case, stripe patterns with the externally imposed periodicity can be stabilized against coarsening above some critical modulation amplitude. However, two essential questions were raised by this model. First, the diffusion-dominated model may not produce the vast Zebra rocks formation argued by Wang et al. (2015). Fluid transport should be necessary for this giant Zebra rock to form across several kilometers horizontally. Second, while the previous model can produce banded and spotted patterns when varying diffusion coefficient or solute mobility, it cannot generate the variable bands photographed in the field, containing horizontal, oblique, and vertical stripes. Thus, we investigate whether directional quenching can create the observed Liesegang-like patterns. This transport-limited model concentrates on the phase separation process by neglecting the diffusion of the reactants and focusing on the dominant fluid flow. Consequently, we investigate whether the fluid transport velocity and initial conditions uniquely determine the pattern morphology.

The phase separation process with advection, where fluid flow transports different components, can generate a wide variety of self-organized patterns in various systems. These include binary alloys, fluid mixtures, polymer blends, and even nanostructured thin films. In material science, controlling this process is crucial for designing nanomaterials and nanodevices with specific functionalities. For example, researchers can create regular structures desirable for applications ranging from bioactive implants to polymer electronics. In such studies Furukawa (1992) investigated the transition between different morphologies (shapes) in a binary mixture by varying the speed of the quenching front, the boundary between the separated phases. They observed and classified three main categories: irregular, regular lamellar (layered), and regular columnar morphologies. Since then, researchers have introduced alternative descriptions for these transitions, considering factors like dimensionality (2D vs. 3D) (Ishikawa et al., 2022), boundary and temperature effects (B. Liu et al., 2000; Ishikawa et al., 2022), and the underlying mechanisms governing the transitions (Krekhov, 2009; Tsukada & Kurita, 2020).

In this contribution we extend the analysis to decipher the geological environments by interpreting geological patterns, particularly pattern formation in Zebra rocks. Although the advection-dominated phase separation model is successfully applied in material science, there are still several research gaps in adopting it in geological pattern formation: (i) the mechanism of oblique patterns, one of the most notable patterns, remains unclear; (ii) the morphological transition from one particular pattern to the oblique pattern is unexplained; (iii) Liesegang patterns are not replicated by the advection-dominated phase separation even though it commonly occurs in diffusion-dominated formulations; (iv) the association between the migration velocities and the band thickness of the uniform patterns remains unclear; (v) the plausibility of deriving geological environments by reproducing the pattern appearance in Zebra rocks needs investigation. We seek to fill these research gaps by adopting the working hypothesis of Kawahara et al. (2022) and studying the phase separation of Fe-oxyhydroxide under acidic Fe-bearing fluid transport conditions by performing numerical simulations in a two-dimensional setting. Note that the model is not limited to the choice of the specific phase separation reaction. However, if a reaction can be identified, the normalized velocities and concentrations can be quantified further by comparing them to laboratory results of the particular reaction chosen. We focus here primarily on the investigation of the effect of the transport velocity and initial Fe-oxyhydroxide concentration on the pattern selection and transitions.

The remaining parts of this study are organized as follows. Section 2 presents the Cahn-Hilliard formulation with the convection term, which can capture the phase separation process during mineral precipitation. In Section 3, we first select numerical pa-

rameters through a series of convergence studies, and then we conduct parameter studies regarding the transport velocity and initial Fe-oxyhydroxide concentration to investigate the pattern selection and transition, especially detailed studies for three different banded patterns. Eventually, we invert the potential geological pattern by replicating the field patterns photographed in a few Zebra rock outcrops. Section 4 discusses our numerical results and suggests potential applications of our model in the future. Finally, we conclude our study in Section 5.

2 Methodology

2.1 Cahn-Hilliard model

We adopt a classical Cahn-Hilliard model to study Liesegang-like pattern formation in a reaction-advection-diffusion system $A_{(aq)} + B_{(aq)} \rightarrow C_{(s)}$. In our study, two reagents A and B denoting Fe-bearing acidic fluid and dolomite, respectively, in our study, react and produce C (i.e., Fe-oxyhydroxide). This model captures the phase separation dynamics occurring in the wake of the fluid front with the A+B chemical reaction. We focus on pattern formation and transition by simulating the dynamics of the phase-separating chemical C in our model instead of including its production as we studied in our previous model (C. Liu et al., 2023a). Using this model, the reaction product C can be separated into low- and high-concentration phases (Antal et al., 1999). The concentration contrast between phases leads to the forming of precipitation patterns. In this study, the Fe-oxyhydroxide concentration enters an unstable region (a.k.a. spinodal), where it divides into a low-concentration region (no precipitate) and a high-concentration region (precipitate), which is underpinned by the classical Cahn-Hilliard equation (Cahn & Hilliard, 1958; Cahn, 1961):

$$\frac{\partial c}{\partial t} = -\nabla \cdot \left(\lambda \nabla \frac{\delta F}{\delta c} \right) \tag{1}$$

where c is the concentration of the reaction product C and λ is the diffusive mobility; we assign $\lambda = 1$ in current study. Let $\mu = \delta F/\delta c = I_c' + B_c'$ be a generalized thermodynamic potential that drives the phase separation. The interfacial energy is

$$I_c = \frac{1}{2}\sigma |\nabla c|^2 \tag{2}$$

in which σ is a constant relevant to interface sharpness; we set it to $\sigma = 0.5$.

In addition, again for simplicity, we use a Landau-Ginzburg type free energy density with two minima corresponding to c_l and c_h and the maximum to $\bar{c} = (c_l + c_h)/2$.

$$B_c = \frac{\varepsilon}{2}(c - \bar{c})^2 - \frac{\gamma}{4}(c - \bar{c})^4 \tag{3}$$

where ε and γ are system-dependent parameters. Here, we assume $\gamma = 1$ and vary the parameter ε to control the phase separation process. When $\varepsilon < 0$, the system is stable with a single minimum; when $\varepsilon > 0$, the system experiences phase separation with two minima. We simply mimic the transport of the Fe-bearing acidic front by varying the parameter ε. Initially, we set $\varepsilon = -1$ in the whole system as the static state before the Fe-bearing acidic front reaches. During the reactive transport process, the parameter ε varies over both time and space as follows:

$$\varepsilon = \begin{cases} -1, & \text{if } x < vt \\ 1, & \text{if } x \geq vt \end{cases} \tag{4}$$

where v is a constant velocity denoting the transport of the Fe-bearing acidic fluid front and t is time.

Finally, by substituting the chemical potential equations (2) and (3), the Cahn-Hilliard equation (1) becomes

$$\frac{\partial c}{\partial t} = \nabla \cdot \left(\lambda \nabla (-\varepsilon c + \gamma c^3 - \sigma \Delta c) \right) \tag{5}$$

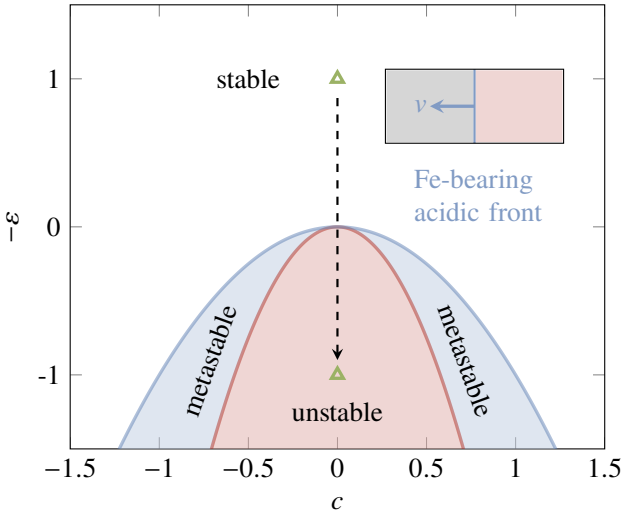

Figure 2. Qualitative phase diagram for the phase separation. Phase separation takes place when $\varepsilon > 0$. The system becomes unstable as $|c| < 1/\sqrt{3}$, while the system is metastable when $|c| > 1/\sqrt{3}$. The system initially has a negative $\varepsilon = -1$, but the concentration is in the unstable region. After the Fe-bearing acidic fluid sweeps at constant speed v, we switch $\varepsilon = -1$ to $\varepsilon = 1$. By doing this, the fluid-swept area will experience phase separation, and different patterns will emerge. Adapted from Tsukada and Kurita (2020).

We use a mixed discretization of the system where we avoid the fourth term in the equation (5) by considering the chemical potential μ as an auxiliary variable to facilitate using the standard bilinear finite element space. Then the governing equation (5) separates as

$$\begin{aligned} \frac{\partial c}{\partial t} &= \nabla \cdot (\lambda \nabla \mu) \\ \mu &= -\varepsilon c + \gamma c^3 - \sigma \Delta c \end{aligned} \tag{6}$$

2.2 Problem statement

We consider an initial-boundary value problem in a rectangular domain Ω as displayed in Figure 3. The domain size is $L_x = 64$ in height and $L_y = 32$ in width, sufficiently large to present different categories of patterns. We impose periodic boundary conditions on the top and bottom edges for both concentration and chemical potential and use the natural boundary condition on the lateral edges. Initially, the product C concentration is set to the stable magnitude, $c_0 = c_{\text{in}} + \eta$ in the whole region, where η denotes noise effects, such as the heterogeneous reagents and thermal fluctuations. We assume η as a random distribution in the range $[-0.01, 0.01]$, a typical value for homogeneous phase-separation simulations (Foard & Wagner, 2012). We put the position of the Fe-bearing acidic fluid front at $x = L_x$. As a result, the whole domain initially remains stable. After the front moves left, the swept region undergoes spinodal decomposition, creating a phase-separating pattern.

After determining the boundary and initial conditions, the governing equations (6) can be solved by PRISMS-PF (DeWitt et al., 2020), which is an open-source, high-performance phase-field code built on a finite element library `deal.ii` (Arndt et al., 2020). Interested readers can derive the weak form based on the Cahn-Hilliard implication. In addition, we use the forward Euler method as the time marching technique. To this end, we should

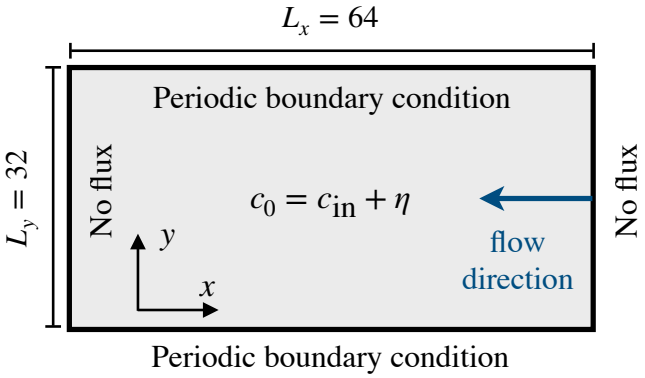

Figure 3. Sketch of initial and boundary conditions for Liesegang-like patterns formation after the infiltration of Fe-bearing fluid flow.

select the time increment satisfying the Courant–Friedrichs–Lewy (CFL) condition, which has been implemented in PRISMS-PF.

3 Results

We use the Cahn-Hilliard model described in Section 2 to numerically study the phase separation phenomenon observed in a geological setting. First, we conduct convergence studies in space and time to choose an appropriate mesh size and time increment in Section 3.1. After selecting the suitable numerical parameters, in Section 3.2, we perform parameter studies on the speed of the Fe-bearing acidic fluid front as well as the initial concentration of the product, which plays a decisive role in selecting the morphology appearance. Finally, Section 3.3 reproduces the different patterns observed in Zebra rocks by the numerical simulations.

3.1 Model convergence study

We demonstrate PRISMS-PF's capability for simulating phase separation problems by conducting convergence studies in space and time. We perform two simulations for the mesh size h selection with a fixed time increment $\Delta t = 1.25 \times 10^{-5}$. We vary the mesh size as $\Delta h = 0.125$ and $\Delta h = 0.25$, respectively. The selections ensure the typical value, i.e., $\sigma/\Delta h$ ranging from 2 to 4, for the phase field methods capturing the structure and interfacial evolution. Figure 4a shows that the resulting patterns are similar except for the localized noise emerging in the transport front. This is because the noise term is introduced in the initial concentration distribution. Meanwhile, the band locations match well, demonstrating the noise cannot change the internal characteristics.

Additionally, we select the appropriate time step size by performing the temporal convergence. We fix the mesh size as $\Delta h = 0.25$ but vary the time size as $\Delta t = 10^{-4}$ and $\Delta t = 1.25 \times 10^{-5}$, respectively. The pattern formation after the transport front approaches the left boundary is depicted in Figure 4b. The reduced time step is in excellent agreement with the large time step. These results imply that the time size $\Delta t = 10^{-4}$ is small enough to guarantee converged results.

3.2 Parameter space analysis and patterning

We thoroughly explore the parameter spaces to understand better how parameters affect the pattern formation and transition as the Fe-bearing fluid passes one geological formation. We identify the two main parameters responsible for pattern formation

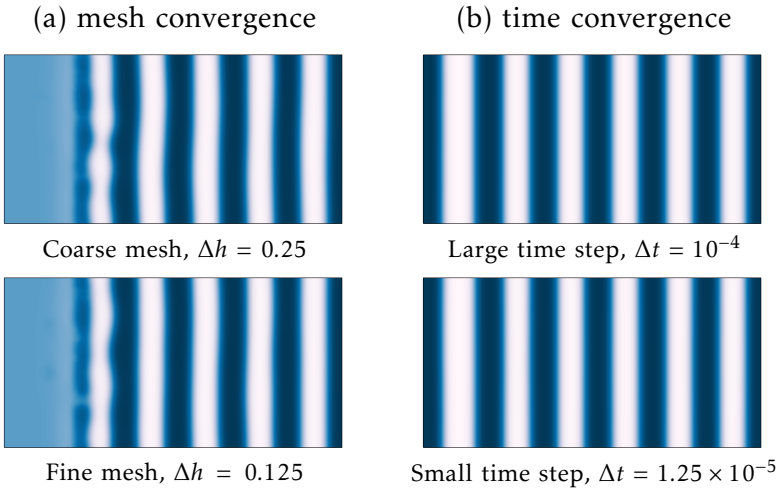

Figure 4. Convergence studies determining numerical parameters: (a) mesh size and (b) incremental time step. Parameters used in these simulations are λ=1, σ=0.5, γ=1, and ε shifting from -1 to 1 after the fluid front passes.

and selection: the fluid velocity v and initial solute concentration c_{in}. We create a phase morphology diagram that illustrates the various patterns by fixing one control parameter constant while adjusting another. From our simulation results, we initially classify these patterns into five morphologies by their characteristics and the formed pattern with the direction of the fluid flow. Subsequently, we assess one category of banded patterns quantitatively by relating the spacing coefficient with the fluid speed. These simulations use the same setup as those described in Section 3.1.

3.2.1 Morphology phase diagram

We numerically examine how the fluid velocity v and initial solute concentration c_{in} influence the pattern evolution. For the parameter sweep, we consider seven different fluid velocities, spanning several orders of magnitude from 0.001 to 10, to ensure the emergence of all potential morphologies. Additionally, we set the initial solute concentration c_{in} from 0.0 to 0.5 with an increment of 0.1, satisfying the spinodal decomposition condition with a limit of $c_{\text{in}}<1/\sqrt{3}$ in Figure 2. As a result, we perform 42 simulations to observe the morphology evolution while varying v and c_{in}, as shown in Figure 5. It is worth noting that we end each simulation as long as the corresponding pattern shows all the characteristics.

First, we classify the patterns that emerge following the phase separation, as the resulting patterns exhibit great versatility. Drawing upon the features exhibited by these patterns, we categorize them as banded or spotted patterns, as discussed in our recent work (C. Liu et al., 2022, 2023a). To avoid any potential confusion, we refer to patterns with a spotty appearance as spotted patterns. Furthermore, within the banded morphologies, we further classify them into three distinct categories based on the direction of the bands relative to the fluid flow: (i) orthogonal bands, characterized by stripes perpendicular to the fluid flow direction; (ii) parallel bands, oriented in parallel with the fluid front; and (iii) oblique bands, displaying an inclined angle relative to the fluid front. Notably, no discernible pattern is observed in some instances referred to as homogeneous cases. In total, our simulations yield five distinct pattern types. Although this simple classification of morphologies is based on our numerical findings, it provides a valuable tool for visually distinguishing patterns observed in geological settings on Earth and Mars (Barge

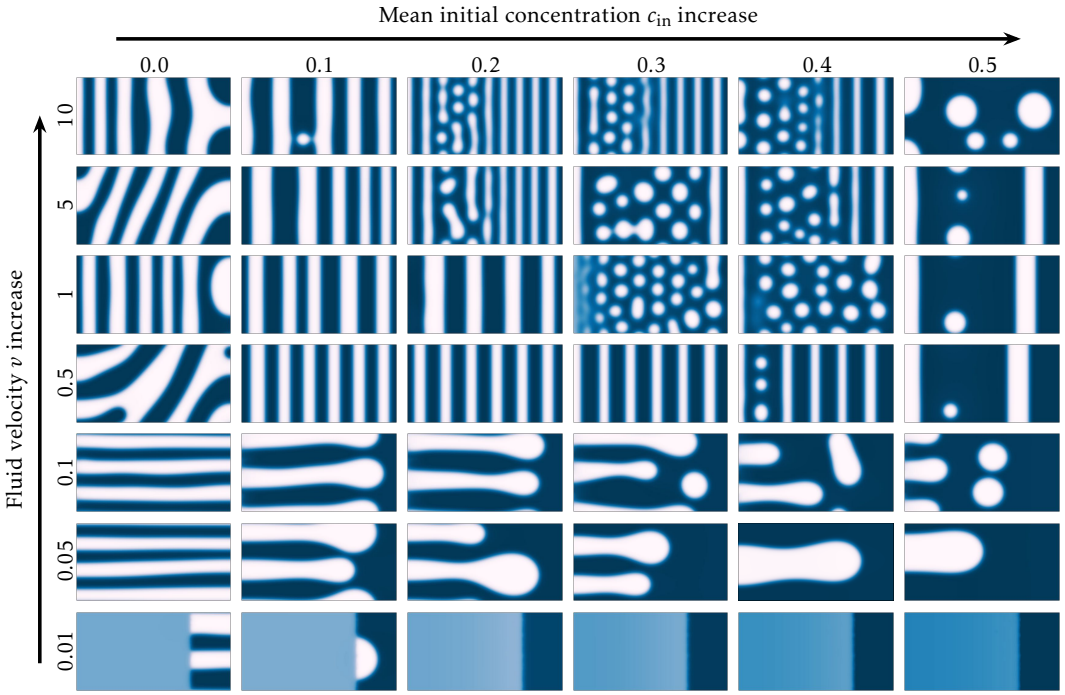

Figure 5. Morphology evolution in the phase diagram where the initial solute concentration and fluid front speed are varied.

et al., 2011; Wang et al., 2015; Yoshida et al., 2018). An example is the patterns observed in Zebra rocks (Coward et al., 2023). According to the proposed classification criterion, we divide the generated patterns into five groups. Figure 6 shows that the fluid velocity v and initial solute concentration c_{in} are crucial to determining the pattern type.

Second, we investigate the effect of the Fe-bearing fluid velocity on the pattern formation and transition as we can observe the simulated patterns from the bottom to top in Figure 6, the simulated patterns transition from parallel bands to orthogonal bands and ultimately to spotted patterns. This transition depends on the initial concentration level c_{in}. The transition speed from the striped to spotted patterns is particularly sensitive to concentration, with the speed decreasing as c_{in} increases. In contrast, when $c_{\text{in}} < 0.5$, the transition speed from parallel to orthogonal stripes is gentler and remains constant throughout our simulations. Without refined simulations conducted, we report the trend that the transition velocity tends to decrease between 0.1 and 0.5 as c_{in} increases. This phenomenon becomes apparent when c_{in} reaches 0.5, and the front velocity v drops from 0.1 to 0.05. Furthermore, homogeneity only arises when the slow velocity is combined with a relatively high initial concentration. Interestingly, oblique bands are only observed once in our phase diagram, with $c_{\text{in}} = 0$ and $v = 0.5$. Given the uniqueness of this pattern, we provide an in-depth analysis in the following section.

Finally, we survey the pattern evolution in the horizontal axis to test the influence of the initial concentration c_{in}. Unlike the comprehensive spectrum of transitions observed when varying the Fe-bearing fluid velocity, changing the concentration c_{in} with a fixed v results in only one discernible transition. However, an exception occurs when $v = 0.5$, where oblique stripes appear when $c_{\text{in}} = 0$. When the transport velocity v is relatively low, pure parallel patterns emerge, while a transition from orthogonal bands to spots is

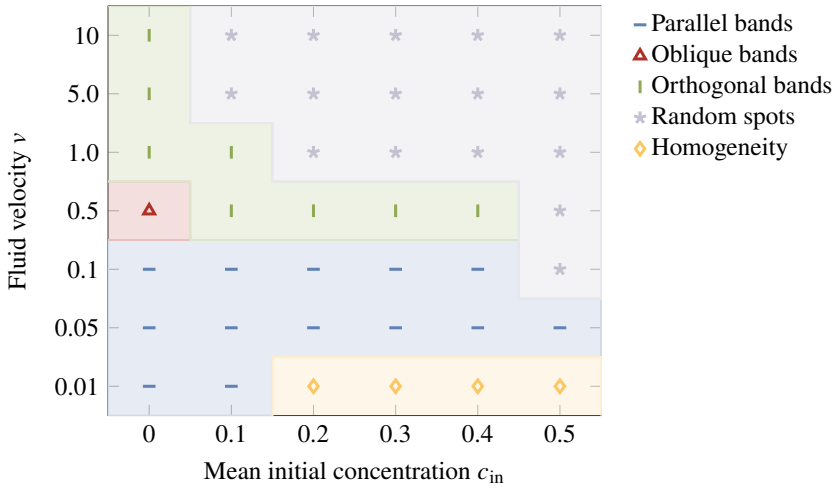

Figure 6. Morphology classification based on the pattern features: homogeneous, banded, and spotted patterns and the banded patterns relative to the fluid direction: parallel, oblique, and orthogonal patterns.

observed at higher velocities. Additionally, either parallel or orthogonal bands evolve into spot morphologies, but a transition between parallel and orthogonal stripes is absent.

3.2.2 Oblique band appearance

Oblique bands appear in a narrow area with the initial solution concentration $c_{\text{in}} = 0$ in the morphology phase diagram. Figure 5 illustrates how the stripe patterns change from parallel to inclined and ultimately to orthogonal bands when the front speed accelerates from 0.1 to 1.0 with a fixed $c_{\text{in}} = 0$. We investigate the transition process by performing extra simulations with v ranging from 0.4 to 0.6 as Figure 7a shows. There, oblique patterns emerge at $v = 0.45$ and $v = 0.5$ but with different inclined directions relative to the fluid front.

The arbitrary occurrence of oblique bands is two-fold. First, the creation of the inclined patterns depends on the competition between the emergence of parallel and orthogonal bands. When the transport velocity reaches a critical value, the competition becomes comparable. As a consequence, the inclined pattern should appear. Second, this competitive mechanism explains the varied angles observed in the phase separation process occurring in an inhomogeneous system. The heterogeneity is realized by the noise term that we add in the initial condition. Figure 7c shows that the noise term can dramatically affect the morphology selection. In these simulations, the randomly distributed noise term is the only changing parameter since we maintain the front velocity $v = 0.45$ constant and vanish the initial concentration. Oblique bands with different directions can appear, even in the form of orthogonal patterns.

The initial solution concentration inhibits the occurrence of oblique patterns. As for the cases of $c_{\text{in}} = 0$, we understand that the oblique patterns develop between the parallel and orthogonal patterns. To test the possibility of inclined patterns when $c_{\text{in}} \neq 0$, we capture the transition process from parallel bands to orthogonal bands as nonzero initial concentrations, e.g., $c_{\text{in}} = 0.1$, as Figure 7b shows. Numerical results show that oblique patterns cannot appear when parallel bands shift to orthogonal bands. The pattern features remain unaltered when we use the same setup as in the convergence stud-

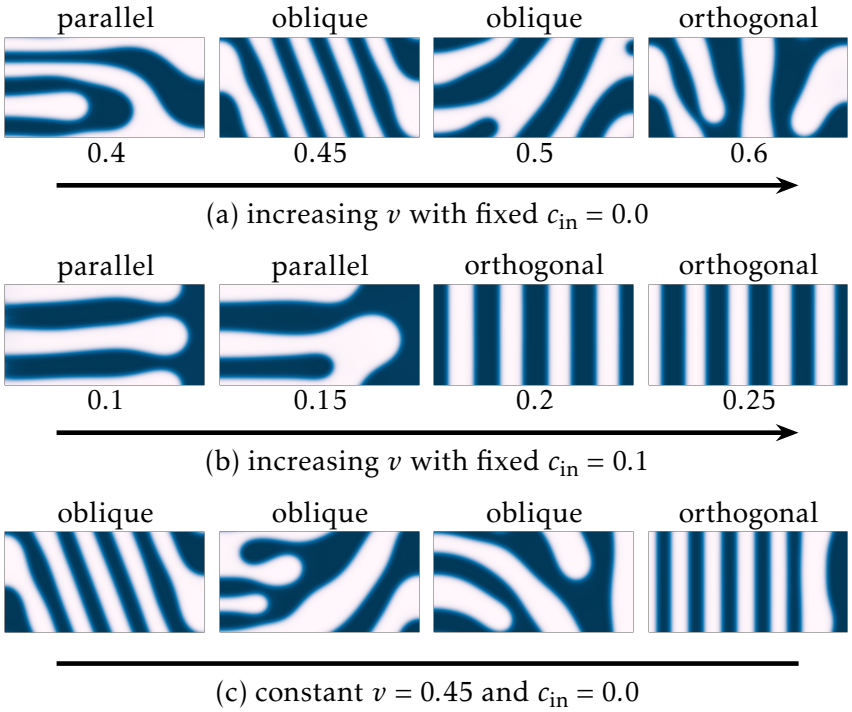

Figure 7. Pattern formation and selection with increasing front speeds and fixed initial solute concentration: (a) c_{in}=0 and (b) c_{in}=0.1. (c) Constant front speed c_{in}=0.45 and concentration c_{in}=0.0 with different .

ies in Section 3.1. This implies that it is the initial concentration that controls the phase separation rather than the additional noise term.

Overall, the vanishing solute concentration plays a pivotal role in determining the appearance of oblique patterns, while the noise effect makes the oblique direction emerge arbitrarily. Our findings explain why randomly oblique patterns can develop in Zebra rocks in the same geological setting (Coward et al., 2023). Specifically, our study suggests that unprecipitated rocks with heterogeneity tend to develop oblique patterns.

3.2.3 Orthogonal patterns with Liesegang phenomenon

In the phase diagram, several orthogonal patterns exhibit characteristics reminiscent of the Liesegang phenomenon. As observed in experiments, Liesegang bands are typically governed by empirical laws regarding their formation time, locations, and widths. The time law cannot apply in our advection-dominated model since the empirical relationships are built in the diffusion-limited experiments. However, we seek to quantitatively validate the Liesegang-like patterns regarding spacing and width laws by focussing on a specific combination of $v = 5$ and $c_{\text{in}} = 0.1$ in Figure 5. This choice is made based on the fact that the simulated patterns exhibit behavior closely resembling Liesegang bands.

Figure 8 presents the product concentration distribution c along the x-axis following the passage of Fe-bearing fluid. As the fluid front propagates, rhythmic precipitation bands appear, forming regular Liesegang band patterns. Qualitatively, the width of periodic stripes and interband spacing increases, consistent with the behavior of Liesegang stripes. We quantitatively verify the empirical laws by measuring the band location, e.g., i-th band location denoted by x_i, and band thickness, e.g., n-th band thickness repre-

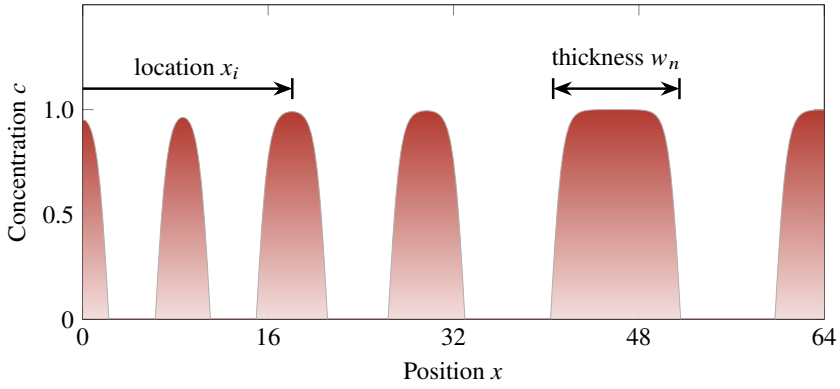

328 **Figure 8.** The product concentration distribution c along the x-axis after the fluid flow, form-
329 ing the regular Liesegang band patterns. x_i and w_n denote location and thickness of the $i-$th
330 and $n-$th bands, respectively.

339 sented by and w_n. The location x_i represents the distance between the band center and
the model boundary.

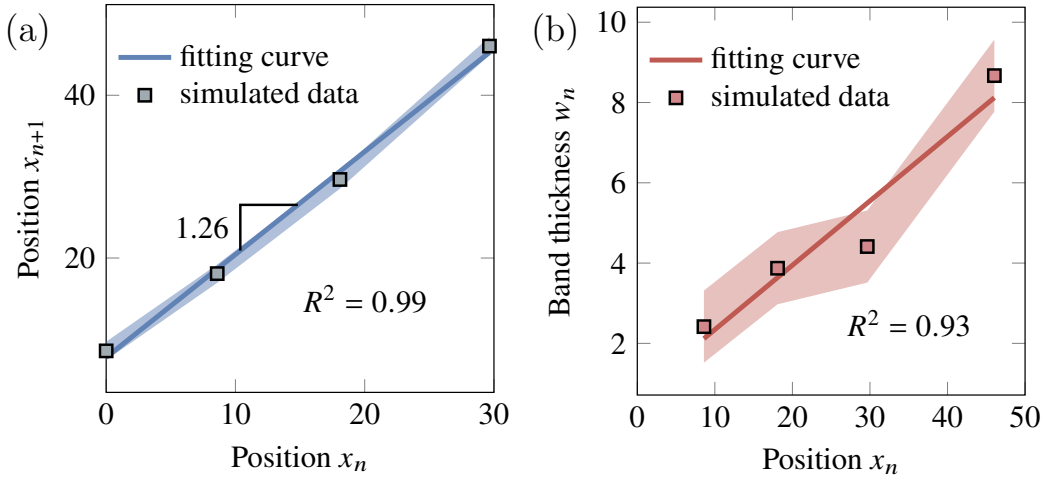

331 **Figure 9.** Verification of Liesegang bands: (a) spacing law and (b) width law. The shaded
332 regions are the liner regression's root mean square error (RMSE).

340

341 We provide quantitative validation for the selected bands and examine the behav-
342 ior of Liesegang striping in terms of the empirical spacing and width laws. The spacing
343 law indicates a linear relationship between the locations of subsequent bands, given by
344 $x_{n+1}/x_n = 1 + p$, where $1 + p$ represents the spacing coefficient. Figure 9a shows this
345 linear relationship, with a high coefficient of determination $R^2 = 0.99$. The estimated
346 value of $1+p$ is approximately 1.26, falling within the 1 to 7 range, consistent with the
347 inversion of Zebra rock samples from the same region (C. Liu et al., 2023a).

348 Additionally, we investigate the width law, which states that the bandwidth w_n is
349 proportional to the position x_n of the band, i.e., $x_n \propto w_n$. Once again, Figure 9b shows
350 a linear relation between x_n and w_n. By successfully reproducing these two empirical

observations from the Liesegang phenomenon, our simplified model demonstrates the ability to replicate Liesegang patterns without considering the diffusion of reactants in the reaction-diffusion system.

3.2.4 Uniform pattern

The uniform pattern, commonly observed in Zebra rocks, suggests that the spacing coefficient is around $1 + p \approx 1$, following the classical Turing pattern (Hu et al., 2022). This study's uniform pattern refers to orthogonal bands exhibiting minimal strip variations. Through our simulations, we discover that the diffusion velocity and the initial concentration influence the bandwidth of each uniform pattern.

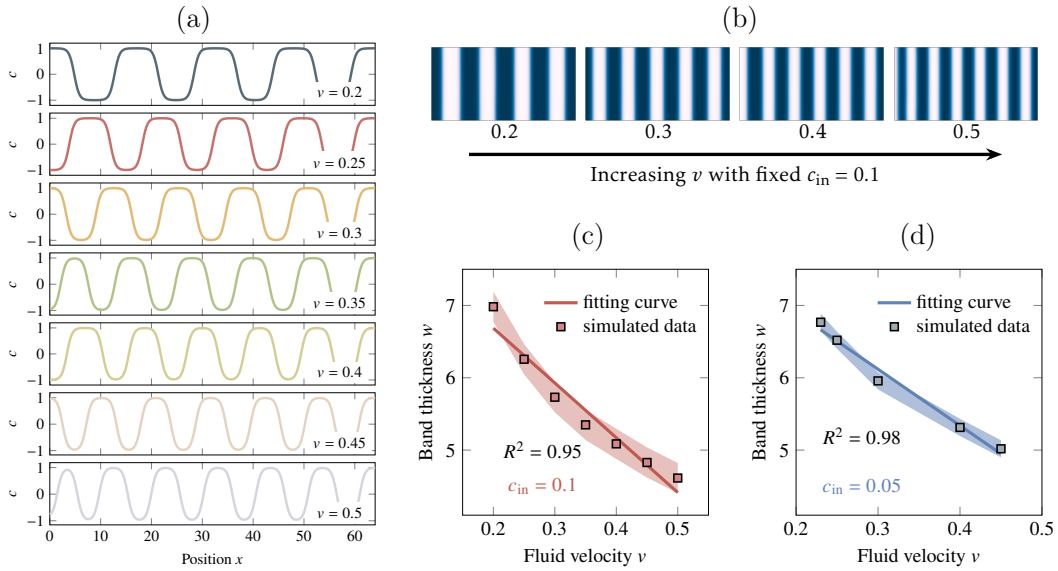

Figure 10. (a) The concentration profiles along the x-axis for varying transport velocities v, ranging from 0.2 to 0.5 with a 0.05 increment, while maintaining a constant initial concentration of c_{in}=0.1. (b) The formation of uniform bands at the end of the simulation for four transport velocities. (c) and (d) The banded thickness measured from the simulations for initial concentrations c_{in}=0.1 and c_{in}=0.05, respectively, along with the corresponding linear fit.

We seek to gain a deeper understanding of the relationship between fluid speed and band thickness; thus, we conduct refined simulations in the phase diagram, varying the fluid speed v from 0.2 to 0.5 with 0.05 increments while maintaining a constant initial concentration of $c_{\text{in}} = 0.1$. Figure 10a shows the concentration profiles along the x-axis, where the bands are located in regions with $c > 0$. Figure 10b illustrates the formation of regular patterns at four different velocities. The repeated bands exhibit nearly identical thickness w_n in each simulation. Therefore, we calculate the average band thickness to assess the generated thickness for different front velocities. Subsequently, we plot the band thickness against the corresponding velocity in Figure 10c. Our results indicate that the band thickness is proportional to the fluid front speed. Specifically, a higher front speed v leads to a decrease in the band thickness w_n, consistent with the finding from Yoshida et al. (2020). We conduct five additional simulations for $c_{\text{in}} = 0.05$ to validate this linear relationship further. In analogy to the case of $c_{\text{in}} = 0.1$, the simulations exhibit the same linear trend as Figure 10d depicts.

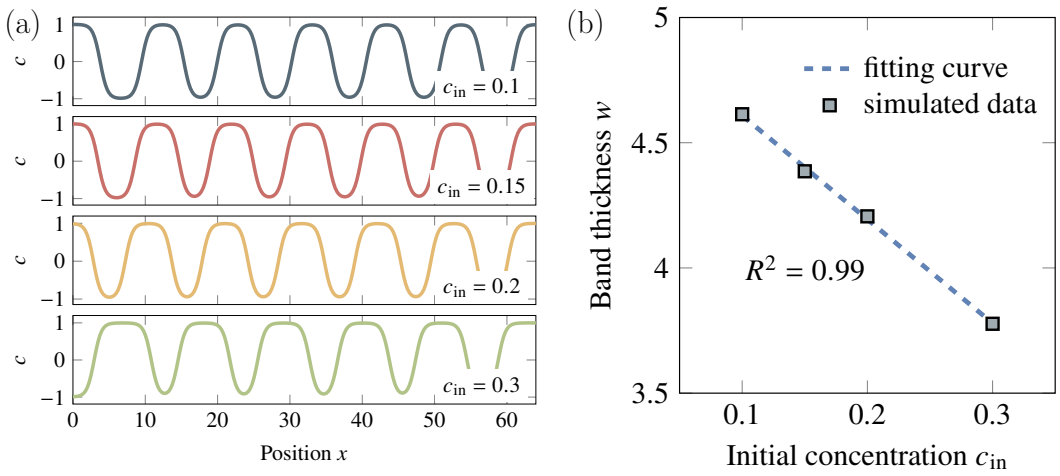

Figure 11. (a) Concentration profiles along the x-axis for four initial concentrations ranging from 0.15 and 0.1 to 0.5 with a 0.1 increment with constant transport velocity v=0.5. (b) The estimated banded thickness from the simulations and the corresponding linear fit.

The transport velocity and the initial concentration influence the thickness of uniform bands. The morphology phase diagram in Figure 5 shows in the column corresponding to $v = 0.5$ for various initial concentrations (c_{in}=0.1, 0.2, and 0.3). We quantitatively investigate this relationship using additional simulations with an initial concentration of $c_{in} = 0.15$ and the same fluid speed of $v = 0.5$. Figure 11a displays the concentration profile along the x-axis, enabling the measurement of the mean band thickness. By determining the average band thickness for each simulation, we can establish a correlation between the parameter c_{in} and the band thickness, as shown in Figure 11b. The band thickness decreases as the initial concentration increases, displaying an almost linear relationship.

3.3 Zebra rock pattern comparison

This section replicates the hematite patterns observed in Zebra rocks from the Western Australian East Kimberley region. We compare the primary features captured by our simulations with those present in the field patterns for different pattern classifications, such as parallel, orthogonal, oblique, and spotted patterns. Our primary focus is to reproduce the diverse morphologies observed in Zebra rocks. However, a quantitative analysis is beyond the scope of the current research. For further details, see our recent work that accurately replicates orthogonal banded patterns in Zebra rocks (C. Liu et al., 2023a).

Parallel bands represent the stripes aligned parallel to the direction of Fe-bearing flow. Field exploration conducted by Coward and co-authors (Coward et al., 2023) in four Zebra rock deposits reveals that this pattern is exclusively observed in the Remote Island outcrop. The researchers identified two representatives within this category: pillars and vertical stripes. Our simulations indicate that these representatives can be classified as parallel bands with varying propagation lengths. We replicate the two Zebra rock samples and determine the corresponding flow speeds and initial concentrations by comparing the simulated morphologies in the morphology phase diagram of Figure 5. The inverted parameters have the same front velocity $v = 0.05$ and the different initial concentrations $c_{in} = 0.5$ for sample 1 and $c_{in} = 0.5$ for sample 2, respectively, as shown in Figure 12.

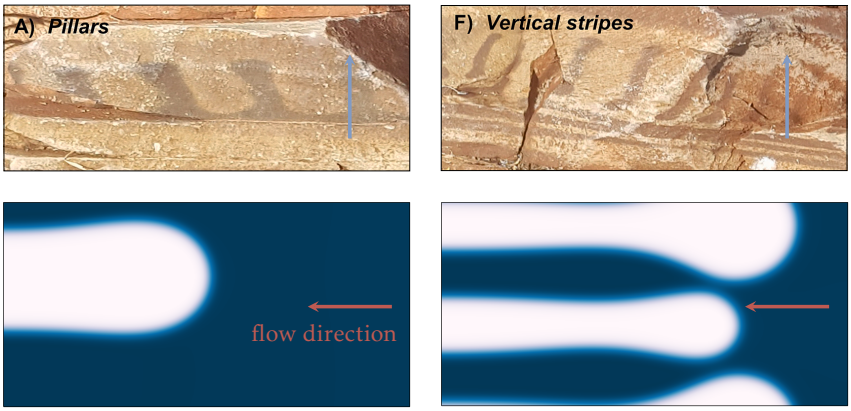

(a) parallel pattern 1 (b) parallel pattern 2

Figure 12. Comparison between the hematite parallel patterns in Zebra rocks and our simulated patterns. The top two Zebra rock samples are from the Remote Island outcrop, adapted from Coward et al. (2023). The arrow denotes the Fe-bearing flow direction in each figure.

Our inversion indicates that parallel bands emerge under conditions of low fluid velocities. The relatively slow fluid velocity, coupled with a high initial concentration, promotes the formation of elongated strips. On the other hand, a low concentration facilitates the development of flat stripes. Consequently, our findings suggest that the transport velocity in the Remote Island outcrop may be relatively sluggish compared to other locations. Furthermore, inhomogeneous initial conditions can give rise to the simultaneous occurrence of both elongated and flat bands.

Orthogonal bands are perpendicular to the fluid direction, commonly observed in various outcrops. Based on field observations, two orthogonal stripes can be distinguished in Figure 13. The first group consists of uniform bands with nearly uniform band thickness, as discussed in Section 3.2.4. The second group comprises Liesegang strips that exhibit an increasing bandwidth along the flow direction, as Section 8 describes.

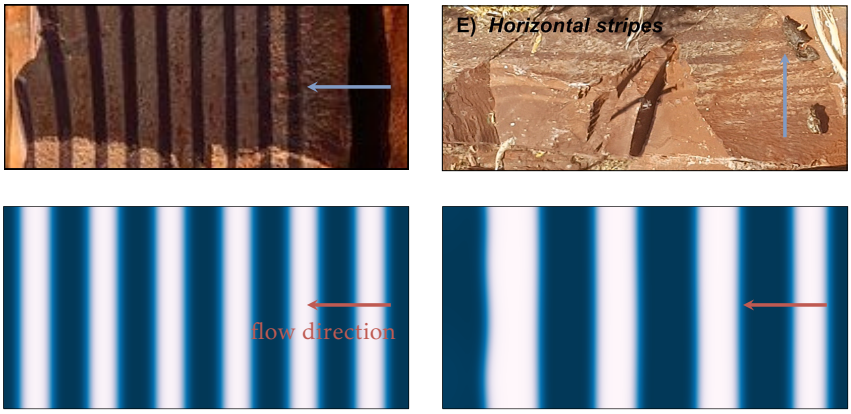

(a) orthogonal pattern 1 (b) orthogonal pattern 2

Figure 13. Comparison between the hematite orthogonal patterns in Zebra rocks and our simulated patterns. The top-right Zebra rock sample is located at the Donkey Road deposit, while the top-right one is from the Remote Island outcrop, adapted from Coward et al. (2023).

Following the same procedure as in the previous comparison, we identify the corresponding orthogonal stripes that resemble the field morphologies in Figure 5. For the uniform bands, parameters $v = 0.5$ and $c = 0.2$ produce a similar pattern as shown in Figure 13. When the velocity is increased to $v = 1.0$ while keeping $c = 0.2$ constant, our simulation results in a Liesegang pattern. Thus, although we compare field and simulated patterns visually, a quantitative analysis is possible, e.g., in C. Liu et al. (2023a). Nevertheless, by exploring the morphology phase diagram in Figure 5, we deduce that the uniform bands indicate a lower transport velocity than the Liesegang patterns. Thus, our study might suggest that the transport velocity for the uniform pattern observed in Donkey Road is lower than that for the Liesegang bands observed in the Remote Island.

Oblique bands are stripes inclined relative to the fluid front, as Figure 14 depicts. The appearance of oblique patterns occurs in field observation and analogous simulations. Previously, we explained this pattern as a consequence of curved diffusion directions (C. Liu et al., 2023a), which could be applicable in specific geological situations. However, this study relaxes the constraint of curved transport velocity for the inclined stripes, allowing them to emerge more efficiently, mimicking a geological setting. Alternatively, the competition between parallel and orthogonal bands could contribute to the forming of oblique bands, as suggested by the transition morphology in Figure 5.

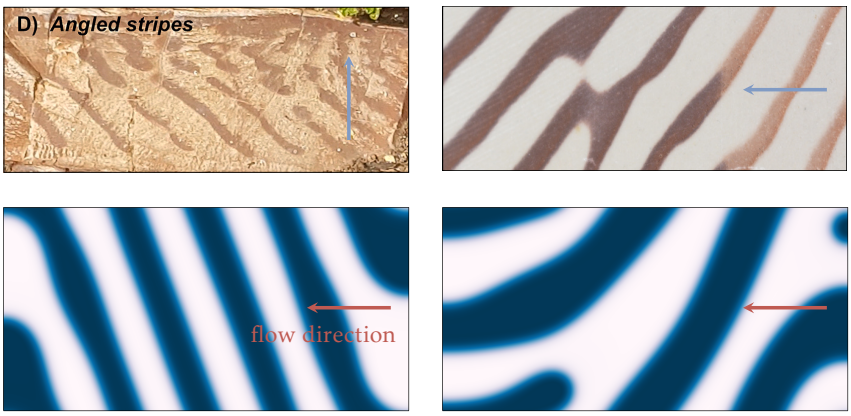

Figure 14. Comparison between the hematite oblique patterns in Zebra rocks and our simulated patterns. The top-right Zebra rock sample is from the Remote Island outcrop (after Coward et al. (2023)), while the top-right one is photographed from the Western Australia Museum.

Next, we investigate parameter combinations for two Zebra rock samples from the Remote Island and the Western Australian Museum. Figure 14 demonstrates that fluid transport velocities of $v = 0.45$ and $v = 0.5$, along with a vanishing initial concentration $c_{\text{in}} = 0.0$, yield comparable oblique bands in the two Zebra rock samples. Interestingly, the field pattern exhibits a branching behavior in some bands, which is also captured in our results in Figure 14b. Furthermore, while two velocities explain different patterns in our study, the presence of oblique patterns is heavily influenced by the noise term η, as Figure 7c shows. Consequently, velocities ranging from 0.45 to 0.5 will likely result in oblique patterns, with the inclined angle pattern depending on the initial noise distribution. Nevertheless, the narrowed range of velocities may provide insight into the potential geological environments during the formation of oblique patterns.

Spotted patterns combine stripes and spots and patterns consisting solely of spots. Figures 15a and 15b depict the two types of spotted patterns: (i) stripes that separate into connected spots and (ii) fully developed isolated spots. Our simulations indicate that higher fluid speeds contribute to the emergence of mixed patterns. Furthermore, the spotted patterns tend to appear when the initial concentration c_{in} falls within the range of 0.2 to 0.4, and the fluid speed v exceeds 0.5.

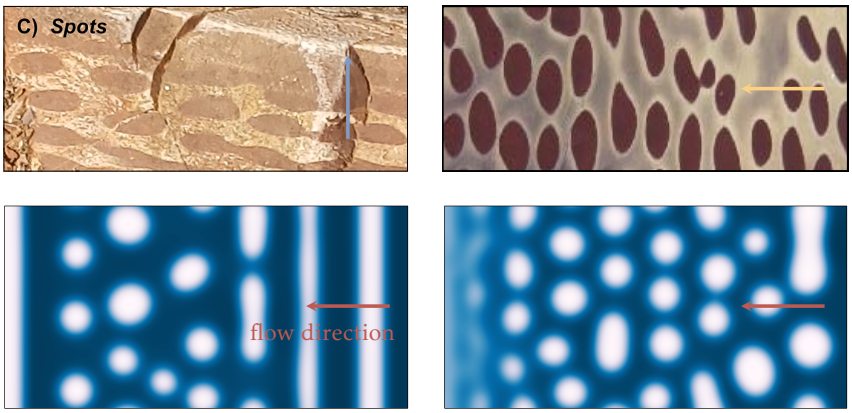

(a) spotted pattern 1 (b) spotted pattern 2

Figure 15. Comparison between the hematite spotted patterns in Zebra rocks and our simulated spots. The top-right Zebra rock sample is from the Remote Island outcrop (after Coward et al. (2023)), while the top-right one is located at the Donkey Load deposit.

Our simulated morphologies determine the optimal parameters to produce morphologies similar to those in the Museum samples are $v = 5.0$ and $c_{\text{in}} = 0.4$ for sample 1 of the Remote Island, and $v = 1.0$ and $c_{\text{in}} = 0.4$ for sample 2 of the Donkey Road. The quantified parameters suggest that the transport velocity in Donkey Road is lower than that for the Liesegang bands observed in the Remote Island. Additionally, our model successfully simulates the Ostwald ripening phenomenon, where the stripes separate into connected and isolated spots in both simulations. This phenomenon plays a crucial role in the pattern transition observed in Zebra rocks, as discussed in our recent work (C. Liu et al., 2023a).

4 Discussion

In this contribution we explored a new framework to explain the diverse patterns observed in Zebra rocks. This framework builds on the idea of self-organization through a process similar to the Liesegang phenomenon, where chemicals organize themselves into bands. Our approach combines the Liesegang theory with a concept from material science called phase separation. We modify a well-established model (Cahn-Hilliard) by adding the effect of flowing groundwater (advection) to mimic how iron oxide dissolves and moves through rock. This improved model successfully reproduces the variety of patterns seen in Zebra rocks. The model reveals that it is important to distinguish these Zebra rock patterns from classic Liesegang bands. Classic Liesegang patterns typically have bands or rings that increase in width and spacing as they move away from their starting point. Zebra rocks, however, exhibit a much wider range of patterns, including bands, rods, and ellipses. We therefore refer to them as Liesegang-like patterns.

For the transport-limited case the observed morphological variations between the Liesegang-like patterns identify differing geological environments during the pattern-forming process, emphasizing just two factors: the initial solute concentration c_{in} and the fluid flow velocity v. By systematically examining the parameter space of c_{in} and v using our model, we can generate all variations of the Liesegang-like patterns previously identified. However, the impact of geological parameters on the band characteristics varies depending on the specific category of Liesegang-like patterns being considered. For example, an oblique banding occurrence most probably indicates the vanishing initial solute concentration before the infiltration of acidic iron-bearing fluids. When the Fe-bearing fluid flow speed narrows to a limited region, the oblique patterns emerge due to the competing growth of orthogonal and parallel bands. Additionally, the arbitrary inclination angles of the oblique bands may be attributed to the heterogeneous geological conditions represented by the noise term when setting the initial solute concentration vanish. Our findings provide insight into the development of randomly oblique patterns observed in Zebra rocks at five outcrop locations (Coward et al., 2023).

One of the categories of orthogonal bands obeys the spacing and width laws commonly observed in traditional Liesegang banding. We have previously replicated this type of pattern, referred to as Liesegang banding, using a pure diffusion-based Cahn-Hilliard formulation. However, we still classify it as a type of Liesegang-like pattern because the advection-based formulation annihilates the time law which is primarily governed by diffusion-limited transport (C. Liu et al., 2022). Our simulations reveal that multiple bands emerge behind the advection front, unlike the classic Liesegang phenomenon, where band thickness increases step by step. The Ostwald ripening process gradually causes neighboring bands to coarsen, eventually leading to characteristics similar to those observed in Liesegang banding.

The existence of a linear correlation between the uniform thickness of orthogonal bands and two controlling parameters presents a valuable opportunity for interpreting the geological context. Our simulations indicate that the band thickness decreases linearly with increasing fluid speed; a similar correlation can be found with the initial solute concentration, too. These quantitative relationships allow us to estimate the fluid flow rates and initial concentrations based on photographic images captured in the field. However, a quantitative comparison of the field patterns with the simulated morphologies is out of the scope of current study. The operational procedure for deriving the diffusion coefficient from orthogonal Zebra rock patterns has been extensively demonstrated in our earlier work (C. Liu et al., 2023a).

The rods and ellipses observed in Zebra rock likely represent an intermediate Ostwald Ripening stage, wherein stripes gradually localize into spots or individual spots coarsen into more prominent spots over time. The former is likely a result of the imposed heterogeneity. At the same time, the latter serves to reduce overall system energy, where combined rods or ellipses are energetically favorable compared to smaller individual spots (Ostwald, 1902). Although our phase separation model can replicate irregular pattern categories, we cannot exclude the possibility of geological deformation occurring after pattern formation (Sheldon & Retallack, 2001; Retallack, 2021). For instance, formation compaction may cause spheroids to reduce, resulting in an elliptical shape, a common occurrence in geological settings. Additional field and experimental work is necessary to confirm the potential impact of compaction on pattern formation.

The examined Zebra rock outcrops exhibit distinct pattern features that have the potential to provide valuable information about chemical conditions and iron transport. First, parallel and orthogonal patterns can be observed in different layers of the Ranford formation, attributed to variations in the infiltrating flow rate into the rock. Referring to the morphology phase diagram (see Figure 5), we can interpret that the fluid flow rate in the parallel banding layer is lower than that in the orthogonal layer. Material heterogeneity, such as permeability, may contribute to these differences in flow rate,

as the patterns are bounded by bedding planes. Similarly, inhomogeneous initial conditions can give rise to the simultaneous occurrence of both elongated and flat bands observed in the Remote Island. Furthermore, the variations in pattern features can be used to infer the flow conditions during the pattern formation process.

Zebra rocks, while beautiful and often used as decorative stones, hold a deeper secret. Understanding the patterns of hematite (iron-oxide) within them can unlock valuable geological information. These patterns reveal the complex interplay between chemical reactions and fluid movement that shaped the rock. Similar processes may have been at work in the distant past, creating features like the early Earth's banded iron formations (BIFs) and the hematite spherules found on Mars. For instance, iron oxide spots and rods found in Earth's Navajo Sandstone are considered a close match to hematite nodules on Mars (Chan et al., 2004; Yoshida et al., 2018). The insights gained from studying Zebra rocks may therefore provide valuable tools for interpreting data and potentially even detecting signs of past life on Mars.

The Precambrian Banded Iron Formations (BIFs) show three scales of bandings that may have self-organizational origins (Wang et al., 2009). Understanding how Zebra rock patterns form has significant implications beyond just Zebra rocks themselves. It can help us unlock secrets about Earth's history and potentially guide resource exploration. BIFs, similar to Zebra rocks in pattern formation but with a higher iron content, are commercially valuable for iron ore. By studying Zebra rocks with our model, methods that identify promising BIF deposits using aerial photographs or drone images may be developed. This could be a game-changer for resource exploration. The abundance of BIFs in the Archaean and early Proterozoic eras, followed by their decline, suggests a significant shift in the ocean environment. Using our simulations to translate observed patterns into geological parameters guides the potential development of entirely new geophysical tools. These tools could help us reconstruct the conditions on early Earth's crust, offering a glimpse into our planet's distant past.

5 Conclusion

This study delves into the intriguing patterns found in Zebra rocks, focusing on how these patterns form over time. We use a computer model that simulates the separation of iron oxide (hematite) under flowing water (advective phase separation). This model provides valuable insights into how two key factors influence the shapes and transitions of these patterns: (i) how the iron oxide is initially distributed within the rock affects the resulting patterns; (ii) the speed at which water moves through the rock plays a role in shaping the patterns.

Using our simulations, we were able to categorize the resulting patterns (referred to as Liesegang-like patterns) and quantify the influence of the two factors mentioned above. Here are some key findings: (i) we were able to recreate the spacing and width of various Liesegang-like patterns based on the initial iron oxide distribution and water flow velocity; (ii) lower initial iron oxide concentration seems to favor the formation of slanted patterns, and the angle of the slant can reveal information about the rock's internal structure; (iii) for straight, banded patterns, we identified a linear relationship between the controlling factors and the thickness of the bands.

Our classification system allows us to match simulated patterns with those observed in the field. This "reverse analysis" helps us to estimate the key parameters that control pattern formation in different Zebra rock locations. By comparing simulated patterns with real-world observations, we found a close resemblance, suggesting the model's accuracy. This paves the way for a powerful tool: a computer-aided interpretation framework. This tool can analyze patterns captured in field photographs, similar to Zebra rocks. We can then estimate crucial geochemical parameters that were present when the pat-

terns formed, including the chemical makeup and water flow conditions. The model's capability to interpret past environments is particularly valuable for understanding the conditions on early Earth and Mars. By analyzing patterns in rocks from these locations, we can potentially uncover clues about the chemical conditions and fluid movement that existed billions of years ago.

6 Open Research

The Finite Element Method code and numerical results will be available after peer review.

Acknowledgments

The authors wish to acknowledge the generous support of the Western Australian Museum for the supply of the high quality images of Zebra Rock in particular Geoff Deacon for taking the photos and the curator Peter Downes for managing the request. The support of the Research Grant Council of Hong Kong (ECS 27203720 and GRF 17206521) and the Australian Research Council (ARC DP200102517, DP170104550, LP170100233) is acknowledged.

References

Al-Ghoul, M., & Sultan, R. (2019). Simulation of geochemical banding: Theoretical modeling and fractal structure in acidization-diffusion-precipitation dynamics. *Physical Review E*, *100*(5), 052214.

Antal, T., Droz, M., Magnin, J., & Rácz, Z. (1999). Formation of Liesegang patterns: A spinodal decomposition scenario. *Physical Review Letters*, *83*(15), 2880.

Arndt, D., Bangerth, W., Blais, B., Clevenger, T. C., Fehling, M., Grayver, A. V., ... Wells, D. (2020). The `deal.II` Library, Version 9.2. *Journal of Numerical Mathematics*, *28*(3), 131-146.

Arvidson, R., Squyres, S., Bell III, J., Catalano, J., Clark, B., Crumpler, L., ... others (2014). Ancient aqueous environments at Endeavour crater, Mars. *Science*, *343*(6169), 1248097.

Barge, L., Hammond, D., Chan, M., Potter, S., Petruska, J., & Nealson, K. (2011). Precipitation patterns formed by self-organizing processes in porous media. *Geofluids*, *11*(2), 124–133.

Cahn, J. W. (1961). On spinodal decomposition. *Acta Metallurgica*, *9*(9), 795-801.

Cahn, J. W., & Hilliard, J. E. (1958). Free Energy of a Nonuniform System. I. Interfacial Free Energy. *The Journal of Chemical Physics*, *28*(2), 258-267.

Chan, M. A., Beitler, B., Parry, W., Ormö, J., & Komatsu, G. (2004). A possible terrestrial analogue for haematite concretions on mars. *Nature*, *429*(6993), 731–734.

Coward, A. J., Slim, A. C., Brugger, J., Wilson, S., Williams, T., Pillans, B., & Maksimenko, A. (2023). Mineralogy and geochemistry of pattern formation in zebra rock from the East Kimberley, Australia. *Chemical Geology*, *622*, 121336.

DeWitt, S., Rudraraju, S., Montiel, D., Andrews, W. B., & Thornton, K. (2020). PRISMS-PF: A general framework for phase-field modeling with a matrix-free finite element method. *npj Computational Materials*, *6*(1), 1–12.

Foard, E., & Wagner, A. (2012). Survey of morphologies formed in the wake of an enslaved phase-separation front in two dimensions. *Physical Review E*, *85*(1), 011501.

Furukawa, H. (1992). Phase separation by directional quenching and morphological transition. *Physica A: Statistical Mechanics and its Applications*, *180*(1-2),

128–155.

Geidans, L. (1981). Zebra rock of Western Australia. In *Geological Society of Australia, Abstracts* (Vol. 3, p. 22).

Hu, M., Sun, Q., Schrank, C., & Regenauer-Lieb, K. (2022). Cross-scale dynamic interactions in compacting porous media as a trigger to pattern formation. *Geophysical Journal International*, *230*(2), 1280-1291.

Ishikawa, R., Tani, M., & Kurita, R. (2022). Three-dimensional phase separation under a nonstationary temperature field. *Physical Review Research*, *4*(3), 033152.

Kawahara, H., Yoshida, H., Yamamoto, K., Katsuta, N., Nishimoto, S., Umemura, A., & Kuma, R. (2022). Hydrothermal formation of Fe-oxide bands in zebra rocks from northern Western Australia. *Chemical Geology*, *590*, 120699.

Krekhov, A. (2009). Formation of regular structures in the process of phase separation. *Physical Review E*, *79*(3), 035302.

Larcombe, C. (1926). Some rocks from four miles east of Argyle Station, Ord River, King district, Kimberley division. *Geological Survey of Western Australia, Annual Report*, *23*.

L'Heureux, I. (2013). Self-organized rhythmic patterns in geochemical systems. *Philosophical Transactions of the Royal Society A: Mathematical, Physical and Engineering Sciences*, *371*(2004), 20120356.

Liu, B., Zhang, H., & Yang, Y. (2000). Surface enrichment effect on the morphological transitions induced by directional quenching for binary mixtures. *The Journal of Chemical Physics*, *113*(2), 719–727.

Liu, C., Calo, V., Regenauer-Lieb, K., & Hu, M. (2023a). Coefficients of reaction-diffusion processes derived from patterns in rocks. *Journal of Geophysical Research: Solid Earth*, *128*(5), e2022JB026253.

Liu, C., Calo, V. M., Regenauer-Lieb, K., & Hu, M. (2023b). Dendritic growth patterns in rocks: Inverting the driving and triggering mechanisms. *Journal of Geophysical Research: Solid Earth*, *128*(9), e2023JB027105.

Liu, C., Hu, M., & Regenauer-Lieb, K. (2022). Liesegang Patterns Interpreted as a Chemo-Hydromechanical Instability. In *Multiscale Processes of Instability, Deformation and Fracturing in Geomaterials: Proceedings of 12th International Workshop on Bifurcation and Degradation in Geomechanics* (pp. 59–66).

Loughnan, F., & Roberts, F. (1990). Composition and origin of the 'zebra rock' from the East Kimberley region of Western Australia. *Australian Journal of Earth Sciences*, *37*(2), 201–205.

Mattievich, E., Chadwick, J., Cashion, J., Boas, J., Clark, M., & Mackie, R. (2003). Macroscopic ferronomatic liquid crystals determine the structure of Kimberley zebra rock. In *Proceedings of the 27th Annual A&NZIP Condensed Matter and Materials Meeting"* (pp. 1–3).

Ortoleva, P. J., Merino, E., Moore, C., & Chadam, J. (1987). Geochemical self-organization i; reaction-transport feedbacks and modeling approach. *American Journal of Science*, *287*(10), 979-1007.

Ostwald, W. (1902). *Lehrbuch der allgemeinen Chemie* (Vol. 2). W. Engelmann.

Qiu, W. J., Zhou, M.-F., & Williams-Jones, A. E. (2024). Numerical Simulation of the Self-Organizational Origin of Concentrically Zoned Aggregates of Siderite and Pyrite in Sediment-Hosted Massive Sulfide Deposits. *Journal of Geophysical Research: Solid Earth*, *129*(3), e2023JB028101.

Retallack, G. (2021). Zebra rock and other Ediacaran paleosols from Western Australia. *Australian Journal of Earth Sciences*, *68*(4), 532–556.

Sheldon, N. D., & Retallack, G. J. (2001). Equation for compaction of paleosols due to burial. *Geology*, *29*(3), 247–250.

Tsukada, T., & Kurita, R. (2020). Mechanism behind columnar pattern formation during directional quenching-induced phase separation. *Physical Review Research*, *2*(1), 013382.

699 Wang, Y., Chan, M. A., & Merino, E. (2015). Self-organized iron-oxide cementation
700 geometry as an indicator of paleo-flows. *Scientific Reports*, *5*(1), 1–15.
701 Wang, Y., Xu, H., Merino, E., & Konishi, H. (2009). Generation of banded iron
702 formations by internal dynamics and leaching of oceanic crust. *Nature Geo-*
703 *science*, *2*(11), 781–784.
704 Yatsuda, Y., Tsushima, K., Fang, Q., & Nabika, H. (2023). Chemical Model for
705 Pattern Formation in Rocks via Periodic Precipitation of Iron Oxide Minerals.
706 *ACS Earth and Space Chemistry*, *7*(10), 2042–2049.
707 Yoshida, H., Hasegawa, H., Katsuta, N., Maruyama, I., Sirono, S., Minami, M., ...
708 others (2018). Fe-oxide concretions formed by interacting carbonate and acidic
709 waters on Earth and Mars. *Science Advances*, *4*(12), eaau0872.
710 Yoshida, H., Katsuta, N., Sirono, S.-i., Nishimoto, S., Kawahara, H., & Metcalfe, R.
711 (2020). Concentric Fe-oxyhydroxide bands in dacite cobbles: Rates of buffering
712 chemical reactions. *Chemical Geology*, *552*, 119786.